



A Statistical Study of the Magnetic Imprints of X-class Solar Flares

Zekun Lu¹ , Weiguang Cao¹, Gaoxiang Jin¹, Yining Zhang¹ , Mingde Ding^{1,2} , and Yang Guo^{1,2} ¹ School of Astronomy and Space Science, Nanjing University, Nanjing 210023, People's Republic of China; dmd@nju.edu.cn² Key Laboratory for Modern Astronomy and Astrophysics (Nanjing University), Ministry of Education, Nanjing 210023, People's Republic of China
guoyang@nju.edu.cn

Received 2018 March 24; revised 2019 February 2; accepted 2019 April 5; published 2019 May 13

Abstract

Magnetic imprints, the rapid and irreversible evolution of photospheric magnetic fields as feedback from flares in the corona, have been confirmed by many previous studies. These studies showed that the horizontal field will permanently increase at the polarity inversion line (PIL) after eruptions, indicating that a more horizontal geometry of the photospheric magnetic field is produced. In this study, we analyze 20 X-class flares since the launch of the *Solar Dynamics Observatory* in 15 active regions with heliographic angles no greater than 45° . We observe clear magnetic imprints in 16 flares, whereas 4 flares are exceptional. The imprint regions of the horizontal field are located not only at the PIL but also at sunspot penumbra with strong vertical fields. Making use of the observed mass and speed of the corresponding coronal mass ejections (CMEs), we find that the CMEs with larger momenta are associated with stronger magnetic imprints. Furthermore, a linear relationship, with a Kendall's Tau-b coefficient 0.54, between the CME momentum and the change of Lorentz force, is revealed. Based on that, we quantify the back reaction time to be ~ 70 s, with a 90% confidence interval from about 50 to 90 s.

Key words: Sun: coronal mass ejections (CMEs) – Sun: flares – Sun: magnetic fields – Sun: photosphere

1. Introduction

Regarded as a rapid energy release process by virtue of magnetic reconnection in the solar corona (Kopp & Pneuman 1976), major solar flares are usually associated with coronal mass ejections (CMEs). It is known that the long-term evolution of a photospheric magnetic field plays an essential role in storing the energy responsible for the flares. However, because the corona is much more tenuous than the photosphere, it has been thought for a long time that solar flares cannot influence the photospheric magnetic fields, especially in short-term evolution.

The first observational evidence of a rapid/irreversible flare-related change of the photospheric magnetic field was reported by Wang (1992) and Wang et al. (1994). A strong and permanent increase of the magnetic shear at the polarity inversion line (PIL) was found. Subsequently, Wang et al. (2002) found rapid permanent changes of photospheric magnetic fields associated with six X-class flares. A survey covering fifteen major X-class flares undertaken by Sudol & Harvey (2005) concluded that the line-of-sight (LOS) magnetic field always changes during X-class flares. The above studies were based on magnetic fields observed by ground-based telescopes.

Nevertheless, ground-based observations have rarely provided time series of magnetograms covering the flare time with a sufficiently high cadence. On the other hand, previous studies were mostly based on the LOS magnetic field data that are actually a combination of both the horizontal component and the radial one. This makes the interpretation of the results more challenging. This intrinsic limitation was solved with high-cadence photospheric vector magnetic field data (Hoeksema et al. 2014) acquired by the Helioseismic and Magnetic Imager (HMI; Scherrer et al. 2012), which was successfully launched on board the *Solar Dynamics Observatory* (SDO; Pesnell et al. 2012). Since then, many more flare events showing rapid and irreversible imprints on the photospheric magnetic field were found (Petrie 2012, 2013; Sun et al. 2012; Wang et al. 2012a, 2012b; Song & Zhang 2016). Ye et al. (2016) observed the

rapid/permanent change of the photospheric magnetic field in a circular ribbon flare, which is associated with the magnetic reconnection of a three-dimensional magnetic null point (Masson et al. 2009, 2017; Wang & Liu 2012; Liu et al. 2015; Yang et al. 2015). Sun et al. (2017) studied magnetic imprints for a sample of X-class flares using recently released SDO/HMI high-cadence vector magnetograms. The main findings of previous studies are that the horizontal magnetic field tends to increase at the PIL, indicating that the vector magnetic field tends to be more horizontal after flare eruptions. Theoretically, the tether-cutting model (Moore et al. 2001) and the coronal implosion model (Hudson 2000) have been used to explain this process.

Although previous observations have revealed many observational aspects of the imprints of solar flares, the results are still not conclusive, thus more statistical studies are required. A statistical work for 18 flare events from 4 active regions (ARs) was conducted by Wang et al. (2012b). Petrie (2012) studied six major flare events in detail and Sun et al. (2017) investigated nine X-class flares. It should be mentioned that the events in these studies are overlapping and mainly belong to major eruptions from a small number of distinct ARs: AR 11158, 11166, 11283, and 11429. Thus, to avoid selection bias, we conduct a comprehensive survey of all the X-class flares with heliographic angles no greater than 45° since SDO's launch.

As for the cause of the magnetic imprints, Fisher et al. (2012) considered the net Lorentz force acting on the upper solar atmosphere, and equated it (with an opposite direction) with the net Lorentz force acting on the interior of the Sun. Meanwhile, the downward momentum incurred by Lorentz force should equal the upward momentum of the erupting plasma. Based on this theory, Wang et al. (2012b) estimated the CME mass by assuming that the back reaction time is of the order of 10 s. In this work, we investigate the relationship between CME momentum and change of the the Lorentz force, where we will elucidate that a change of the Lorentz force can

serve as an indicator of the strength of the magnetic imprint. Moreover, instead of an empirical estimation, we give a more exact evaluation of the reaction time, which is an important parameter for understanding the reaction process.

Our motivations for this study are fourfold: (1) to investigate the general properties of flares' imprints on the photosphere; (2) to figure out the location of the imprints and categorize them; (3) to quantitatively describe the change of magnetic field including horizontal field change and inclination angle change; and (4) to further study the relationship between CMEs and the imprints on the photosphere. In Section 2, we describe the observations and the data processing procedure for 20 events with AR 12242 as an example. The statistical results for the magnetic field change are presented in Section 3, together with the relationship between the CME momentum and the change of Lorentz force. In Section 4 we discuss and summarize our findings.

2. Observation and Data Reduction

For the events occurring near the solar limb, when compared with those near the disk center, the observational noise level is typically higher; moreover, it is harder to spatially resolve small structures of solar flares because a pixel covers a larger area of the solar surface. Therefore, to guarantee the reliability of our study, we only study the near-disk center X-class flares with heliographic angles no greater than 45° . We scrutinize the whole list of X-class flares,^{3,4,5} from *SDO*'s launch in 2010 to 2017 June 28, and select 20 flare events from 15 ARs (listed in Table 1). The *GOES* X-ray classes of the sample flares range from X1.0 to X5.4, making this to date the largest sample for studying magnetic imprints of X-class flares since *SDO*'s launch. Most importantly, we do not use any other subjective selection criteria other than setting a threshold for the flare class and heliographic angle of the flare site, which avoids bias in the statistical results.

The HMI and Atmospheric Imaging Assembly (AIA; Lemen et al. 2012) on board *SDO* provide full-disk vector magnetic fields and Extreme Ultraviolet images, respectively, with high spatial and temporal resolutions. More specifically, we trace the morphology of flare ribbons using the AIA images at wavelength 1600 Å, with a cadence of 24 s (aia.lev1_uv_24s⁶). HMI acquires full-disk photospheric magnetograms with a pixel size of $0''.5$ at a cadence of 12 minutes. The magnetic field is inverted from the Stokes parameters at six wavelengths distributed around the photospheric Fe I 6173 Å line.⁷ The 180° azimuthal ambiguity is resolved through the “minimum energy” method (Metcalfe 1994; Leka et al. 2009). The noise level of the LOS field measurement is about 10 G; the noise level of the transverse field is of the order of 100 G (Liu et al. 2012). In this work, we use the vector magnetogram Spaceweather HMI Active Region Patch (SHARP), where the ARs are automatically identified and extracted. We obtained the three components of the vector magnetic fields, B_r , B_p , B_t from the deprojected maps provided in the cylindrical equal area coordinate system (hmi.sharp_cea_720s;⁸ Bobra et al. 2014).

As mentioned above, solar flares' imprints on the photosphere are mainly reflected by the irreversible increase of horizontal magnetic field, $B_h = \sqrt{B_p^2 + B_t^2}$, at the PIL. Thus, for all events under study, we merely focus on the regions with magnetic field changes that meet two criteria:

1. A significant increase of B_h is detected during the solar flare. To avoid unreal enhancement of B_h arising from noise, we set a threshold of increase, 100 G, the contour of which is marked in yellow.
2. The increase of B_h is temporally associated with solar flares. To get rid of non-flare-associated field changes, such as emerging flux or moving magnetic features (see Hagenaar & Shine 2005; Iida et al. 2012), we also calculate the change of B_h in the post-flare stage, defined at an equal duration interval starting three hours after the start time of the flare. If B_h increases during the flare but does not increase after the flare, the increase is regarded to be associated with solar flares. The boundary of the flare-associated increase of B_h is marked by red or blue boxes.

Therefore, we define the regions of interest (ROIs) as the regions that meet both criteria above; visually, the ROIs are the colored areas inside the boxes.

To demonstrate the procedure of data processing, we take the analysis of the sample with the most complex imprint as an example: the X1.8 flare in AR 12242. First, we scrutinize the evolution of the horizontal field and plot the difference map between flare start time and end times (defined based on the recorded start and end times of *GOES* soft X-ray emission), as is seen in Figure 1(c). Second, as seen in Figures 1(a) and (b), we plot the radial magnetic field, B_r , as the background on which the regions with difference values, δB_h , greater than 100, 200, and 300 G, are marked in yellow, orange, and red, respectively. Panel (a) shows the difference map during the flare, while panel (b) shows the difference map three hours after the flare. Here, with a focus on the rapid/irreversible change of B_h during flare time, we consider the post-flare change as the non-flare-associated change. Visually, we exclude the non-flare-associated change out of the difference map of B_h in the flare stage, then keep the remaining regions as flare-associated change, as marked by boxes. Therefore, the colored areas inside the boxes in Figure 1(a) are ROIs as defined above. We can see that, unlike the flare-associated change of B_h , the non-flare-associated change of B_h is dispersed across the whole field of view. Considering its low amplitude and small area, we regard the non-flare-associated change as mostly noise or computational errors. In particular, we point out that the increase of the horizontal field appears not only at the PIL, as marked by the red box, but also at the sunspot penumbra region, where $B_r > 1000$ G, as marked by the blue box.

We will show in Section 3 that such a double region increase is not unique. There are other types of magnetic imprints. Third, because we are interested in the spatial relationship between magnetic imprints and flare ribbons, we show the AIA image of the flare region at 1600 Å in Figure 1(d). We can find that, spatially, region R1 is located mainly between the two flare ribbons, whereas region R2 is located partially on the flare ribbon. Note that the coordinates of SHARP maps have been transformed to helioprojective-Cartesian coordinates for comparison with the AIA map. Finally, we plot the evolution of the weighted mean change of the horizontal field and that of the inclination angle within the ROI as a function of time. The

³ <ftp://ftp.ngdc.noaa.gov/STP/space-weather/solar-data/solar-features/solar-flares/x-rays/goes/xrs/>

⁴ <https://www.solarmonitor.org/>

⁵ <https://helioviewer.org/>

⁶ http://jsoc.stanford.edu/ajax/lookdata.html?ds=aia.lev1_uv_24s

⁷ <http://jsoc.stanford.edu/jsocwiki/VectorMagneticField>

⁸ http://jsoc.stanford.edu/ajax/lookdata.html?ds=hmi.sharp_cea_720s

Table 1
List of 20 Flare Events from 15 ARs with Heliographic Angles No Greater than 45°

NOAA AR	Date	GOES Class	Location	Start (UT)	Stop (UT)	Peak (UT)	Category ^a	$\langle \delta B_h \rangle^b$ (Gauss)	$\langle \delta \phi \rangle^c$ (°)	CME Momentum (10 ¹⁷ g km s ⁻¹)
11158	2011 Feb 15	X 2.2	S21W28	01:44	02:06	01:56	Type I	286 ± 59	6.23 ± 0.47	28.77
11166	2011 Mar 9	X 1.5	N11W15	23:13	23:29	23:23	Type I	258 ± 73	2.31 ± 1.13	0.40
11283	2011 Sep 6	X 2.1	N14W18	22:12	22:24	22:20	Type I	339 ± 53	3.70 ± 0.50	86.25
11283	2011 Sep 7	X 1.8	N14W32	22:32	22:44	22:38	Type I	260 ± 66	7.84 ± 0.64	8.71
11302	2011 Sep 24	X 1.9	N13E45	09:21	09:48	09:40	Type I	197 ± 99	10.49 ± 1.65	54.21
11429	2012 Mar 7	X 5.4	N17E27	00:02	00:40	00:24	Type I	216 ± 73	9.30 ± 0.35	375.76
11430	2012 Mar 7	X 1.3	N22E12	01:05	01:23	01:14	Type I	170 ± 95	5.75 ± 0.76	...
11890	2013 Nov 5	X 3.3	S13E44	22:07	22:15	22:12	Type I	454 ± 121	3.51 ± 1.21	26.98
11890	2013 Nov 8	X 1.1	S14E15	04:20	04:29	04:26	Type I	387 ± 56	7.55 ± 0.63	...
11890	2013 Nov 10	X 1.1	S14W13	05:08	05:18	05:14	Type I	285 ± 57	4.10 ± 0.60	15.69
12017	2014 Mar 29	X 1.0	N11W32	17:35	17:54	17:48	Type I	223 ± 63	10.29 ± 0.75	26.40
12205	2014 Nov 7	X 1.6	N17E40	16:53	17:34	17:26	Type I-R1	323 ± 78	8.79 ± 0.82	95.40
							Type I-R2	278 ± 75	7.40 ± 0.83	
12297	2015 Mar 11	X 2.2	S17E21	16:11	16:29	16:22	Type I	309 ± 102	4.00 ± 1.04	2.64
11520	2012 Jul 12	X 1.4	N13W15	15:37	17:30	16:49	Type II-R1	212 ± 33	5.73 ± 0.81	61.06
							Type II-R2	215 ± 88	1.17 ± 0.46	
12158	2014 Sep 10	X 1.6	N15E02	17:21	17:45	17:45	Type II-R1	161 ± 22	5.80 ± 1.56	...
							Type II-R2	167 ± 15	3.67 ± 0.96	
12242	2014 Dec 20	X 1.8	S21W24	00:11	00:55	00:28	Type II-R1	261 ± 58	9.09 ± 0.35	182.60
							Type II-R2	161 ± 39	4.25 ± 0.60	
11944	2014 Jan 7	X 1.2	S12W08	18:04	18:58	18:32	Type III	402.6
12192	2014 Oct 22	X 1.6	S14E13	14:02	14:50	14:28	Type III	0.50
12192	2014 Oct 24	X 3.1	S16W21	21:07	22:13	21:44	Type III	0.0552
12192	2014 Oct 26	X 2.0	S18W40	10:04	11:18	10:56	Type III

Notes.^a The category is defined in Section 3.^b The weighted mean changes of horizontal field B_h and inclination angle ϕ are defined by Equations (1) and (2).^c The CME momenta are computed by multiplying the CME mass and CME speed.

definitions of these parameters are as follows:

$$\langle B_h \rangle = \frac{\sum_{\text{ROI}} |\mathbf{B}| \cdot B_h}{\sum_{\text{ROI}} |\mathbf{B}|}, \quad (1)$$

$$\langle \phi \rangle = \frac{\sum_{\text{ROI}} |\mathbf{B}| \cdot \phi}{\sum_{\text{ROI}} |\mathbf{B}|}. \quad (2)$$

Here, for better comparison with previous studies, we follow the definition of the magnetic inclination angle ϕ in Wang et al. (2012a): $\phi = \arctan \frac{B_r}{\sqrt{B_\theta^2 + B_\phi^2}}$. As shown in Figures 1(e)–(h), both $\langle B_h \rangle$ and $\langle \phi \rangle$ show a stepwise change in 40 minutes, which is consistent with previous findings. It is worth pointing out that because of the flare heating, the inversions of Stokes profiles are generally not reliable during the flare (Hong et al. 2018), which further brings uncertainty to the magnetograms of HMI. Nevertheless, inversions of Stokes profiles are reliable before and after the flare, during which the quantities B_h and ϕ almost keep constant. Thus, despite the uncertainty during the flare, the irreversible/stepwise change of B_h and ϕ seems realistic. We also compare the region at the PIL and the region at the penumbra. It is found that the changes of the horizontal field are similar in the two regions; however, the change of the inclination angle in the PIL region is greater than that in the penumbra region. This result can be expected due to a stronger B_r field in the latter. Note that the errors in $\langle B_h \rangle$ and $\langle \phi \rangle$ are calculated according to the error transfer formula.

To further reveal the origin of such an irreversible change of the magnetic field, we analyze the relationship between the CME momentum and the Lorentz force change as predicted by Fisher et al. (2012). The change in the vertical component of the net Lorentz force acting on the volume below the photosphere is formulated as

$$\delta F_r = \frac{1}{8\pi} \int_{A_{ph}} dA (\delta B_r^2 - \delta B_h^2). \quad (3)$$

We note that, similar to previous results (Wang et al. 2012b; Song & Zhang 2016; Sun et al. 2017), the vertical field B_r shows no rapid change in the time duration of 8 hr. Therefore, we omit the term δB_r^2 and calculate δF_r in the ROI depending solely on the term δB_h^2 , which means that the Lorentz force change can serve as a reasonable indicator of the strength of the magnetic imprints, namely⁹

$$\delta F_r \approx \frac{1}{8\pi} \int_{A_{\text{ROI}}} dA (-\delta B_h^2). \quad (4)$$

On the other hand, we estimate the CME momentum by directly multiplying the CME mass by the linear speed of the CME as observed by the *SOHO* satellite.¹⁰

⁹ For convenience, the δF_r used in statistical study means the decrease of Lorentz force, which is the absolute value of that in Equations (3) and (4).

¹⁰ https://cdaw.gsfc.nasa.gov/CME_list/

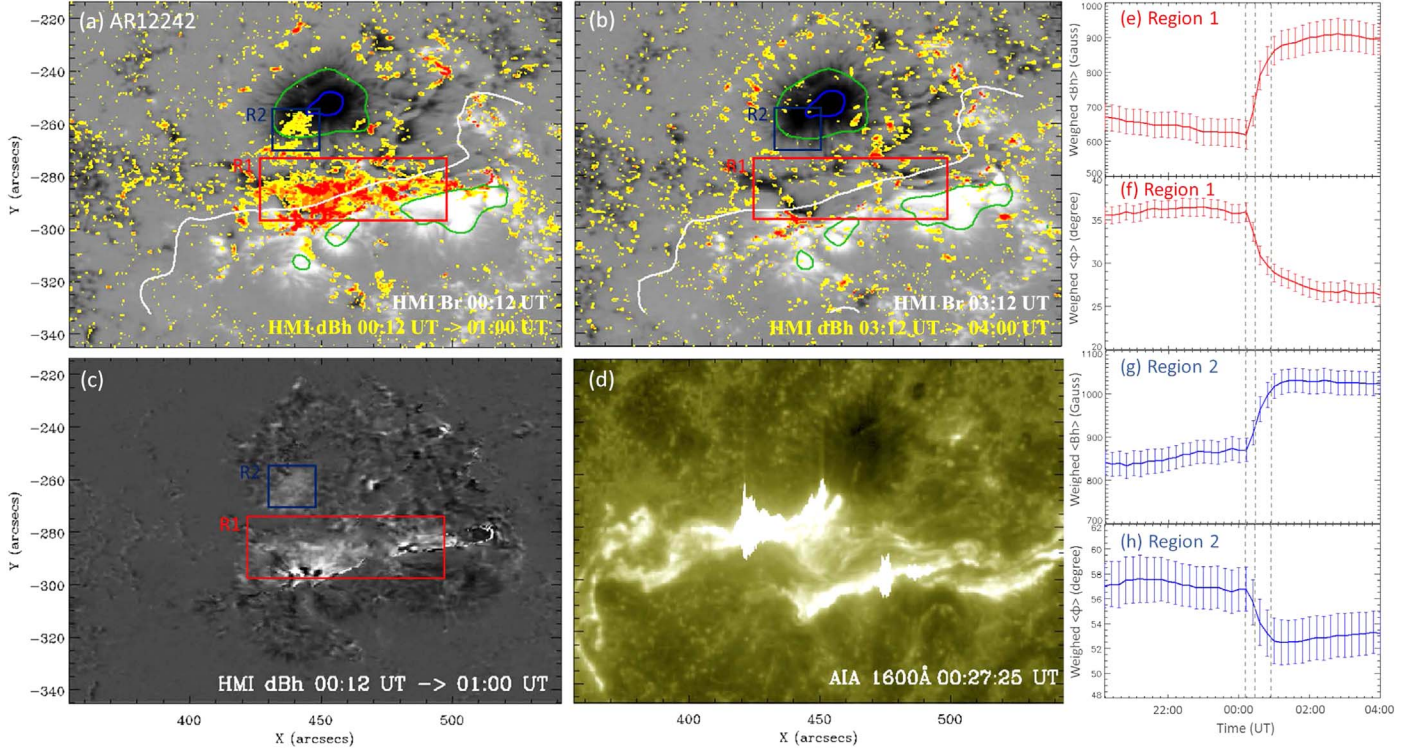


Figure 1. X1.8 flare on 2014 December 20. Panels (a) and (b) show the change in the magnitude of the horizontal field (the color map), $|\delta B_h|$, with a threshold 100 G, during and after the solar flare. The areas with a change, $|\delta B_h|$, greater than 100, 200, and 300 G are marked in yellow, orange, and red, respectively. In panel (a), we show the difference map of B_h in the flare stage (from 00:12 UT to 01:00 UT). In panel (b), we plot the difference map of B_h in the post-flare stage (from 03:12 UT to 04:00 UT, three hours after flare stage). The background gray map shows the radial magnetic field B_r , scaled between ± 2000 G, where $|B_r| = 1000$ and 2000 G are contoured using green line and blue lines, respectively. The white line shows the smoothed PIL, where $B_r = 0$ G. The red box encloses the region (Region 1) with flare-associated enhancement of B_h at the PIL; the blue box encloses the region (Region 2) with such a change at the penumbra. Panel (c) is the difference map of the horizontal field, with contrast strengthened. Panel (d) is an AIA 1600 Å map around flare peak time. In panels (e)–(h), we plot the 8 hr evolution of the weighted mean horizontal field and weighted mean magnetic inclination of ROI (the colored areas inside Region 1 and Region 2), where the gray dashed lines mark the start, peak, and end times of the flare. The vertical error bars are calculated through error transfer formula.

Table 2
List of 13 Flare Events with CMEs in Type I and II

NOAA AR	Date	GOES Class	CME Time ^a (UT)	CME Speed (km s ⁻¹)	CME Mass (10 ¹⁵ g)	CME Momentum ^b (10 ¹⁷ g km s ⁻¹)	δF_r (10 ²² dyne)
11158	2011 Feb 15	X 2.2	02:24	669	4.3	28.77	5.06
11166	2011 Mar 9	X 1.5	23:05	332	0.12	0.40	1.46
11283	2011 Sep 6	X 2.1	23:05	575	15.0	86.25	2.76
11283	2011 Sep 7	X 1.8	23:05	792	1.1	8.71	2.92
11302	2011 Sep 24	X 1.9	09:48	1936	2.8	54.21	1.33
11429	2012 Mar 7	X 5.4	00:24	2684	14.0	375.76	14.1
11520	2012 Jul 12	X 1.4	16:48	885	6.9	61.06	2.87
11890	2013 Nov 5	X 3.3	22:36	562	4.8	26.98	5.53
11890	2013 Nov 10	X 1.1	05:36	682	2.3	15.69	3.21
12017	2014 Mar 29	X 1.0	18:12	528	5.0	26.40	1.44
12205	2014 Nov 7	X 1.6	18:08	795	12.0	95.40	7.66
12242	2014 Dec 20	X 1.8	01:25	830	22.0	182.60	8.77
12297	2015 Mar 11	X 2.2	17:00	240	1.1	2.64	6.18

Notes.

^a Information on the CME time is from the *SOHO* catalog.

^b The CME momenta are computed by multiplying the CME mass and CME speed.

For each X-class flare, we pay attention to a time period of eight hours. We then apply the same procedure to all 20 flare events listed in Table 1. The detailed CME information and the change of the vertical Lorentz force are recorded in Table 2.

3. Statistical Results

Following the same data reduction procedure introduced in Section 2, we are able to plot the magnetic imprints as shown in Figures 2–4.

So far, many authors have given observational evidence of the type of magnetic imprint whose horizontal field irreversibly increased at the PIL (Petrie 2012, 2013; Sun et al. 2012; Wang et al. 2012a, 2012b; Song & Zhang 2016), with a comprehensible physical interpretation (Hudson 2000; Moore et al. 2001; Fisher et al. 2012). However, for other types of magnetic imprints, more observational and theoretical discussions are needed before we can completely understand them. In this sense, according to the spatial distribution of the ROI, more exactly, at PIL or not, we are able to categorize the magnetic imprints of 20 X-Class flares into three types:

1. Type I: B_h increases at the PIL only, where there is a contiguous area of increasing B_h that encompasses a PIL. In these events, we can identify a continuous area with a strong enhancement of the horizontal field covering the PIL and the main flare region revealed by the 1600 Å AIA images, which is in agreement with previous results. Most of the events belong to this type.
2. Type II: B_h increases both at the PIL and the penumbra, where there is a contiguous area of increasing B_h that encompasses a PIL, as well as a contiguous area of increasing B_h inside a penumbra. In a small number of events, besides the area at PIL, we can also identify a continuous area with an enhanced horizontal field at the penumbra, where the vertical magnetic field is greater than 1000 G. The events occurring in AR 11520, AR 12158, and AR 12242 belong to this type.
3. Type III: B_h increases in a separate and irregular way, spatially with little relation to the PIL. Meanwhile, as shown in Figure 4, such changes also occur after the flare, so there is no temporal association with the flare. Although we cannot exclude the relationship between the increases of B_h and solar flares, the colored regions (with an increase of B_h greater than 100 G) are identified as non-flare-related and are mostly from noise or measurement errors. One X-class event in AR 11944 and three events in 12192 belong to this type.

Therefore, we reach the following statistical results: (1) 16 out of 20 events embed clear magnetic imprints; 1 sample in AR 11944 and 3 samples in AR 12192 are exceptional (Type III); (2) among the 16 flares with magnetic imprints, 13 events embed imprints only at the PIL, as reported before, while 3 embed imprints both at the PIL and the sunspot penumbra; (3) the ROI in red boxes (Type I and R1 in Type II) spatially covered the flaring PIL, as revealed by the AIA data; the ROI in blue boxes (R2 in Type II) are located on the flare ribbons.

In addition to the above qualitative results, we perform a quantitative study on the change of the horizontal field, δB_h , and that of the inclination angle, $\delta\phi$, in all marked boxes for the 16 events of Type I and Type II, as well as the parameters for the associated CME events. Note that, considering the poor relation between an increase of horizontal field with solar flares, such quantitative statistics do not include the events in Type III. We calculate the mean values of B_h , ϕ before the flare eruption,¹¹ denoted as $\langle B_h \rangle_{\text{pre}}$ and $\langle \phi \rangle_{\text{pre}}$, and the mean values of B_h and ϕ after the eruption, denoted as $\langle B_h \rangle_{\text{post}}$, and $\langle \phi \rangle_{\text{post}}$. Their difference values, $\langle \delta B_h \rangle$ and $\langle \delta \phi \rangle$, are listed in Table 1. The errors in the table are calculated from an error transfer

formula. Because we are interested in the relationship between the magnetic imprints and the CME, we are able to plot the quantities describing the magnetic imprints independent of the CME momentum. The CME momentum of the flares in AR 11430, AR 11890 (2013 November 8), and AR 12158 are not available, so we do not show the three events in Figure 5. As can be seen in Figures 5(a)–(b), the ratio of change of the horizontal field, $\frac{\langle B_h \rangle_{\text{post}} - \langle B_h \rangle_{\text{pre}}}{\langle B_h \rangle_{\text{pre}}}$, ranges from $\sim 20\%$ to $\sim 80\%$, with an average value of $\sim 40\%$. Note that, given the size of the error bars, except for the events in AR 11166, 12297, and 11520 (R1), the ratio of change of the horizontal field at PIL (red boxes) tends to be a constant of $\sim 40\%$, whereas the ratio of change of the horizontal field at the penumbra (blue boxes) tends to be $\sim 20\%$. We suspect that these high values are due to the fact that all the flares in our sample are X-class. The change ratio should be different in other flares with lower classes. The ratio of change of the inclination angle, $\frac{\langle \phi \rangle_{\text{post}} - \langle \phi \rangle_{\text{pre}}}{\langle \phi \rangle_{\text{pre}}}$, is no greater than 25%. No evident relationship can be seen between the CME momentum and the ratio of change of B_h or ϕ .

So far, there are some limitations to our method. First, our method cannot completely remove the non-flare-associated change from the raw difference map. We visually exclude the non-flare-associated change area by excluding the δB_h at the post-flare stage and that at the flare stage. However, inside the boxes, we cannot remove the non-flare-associated contribution of δB_h from the ROI, which means that the magnetic field change in our statistics may still contain some non-flare-associated changes. Meanwhile, for the events whose magnetic imprints are not completely centralized at the PIL, some changes might be neglected outside the boxes. Second, similar to the definition of ROI in Wang et al. (2012b), our temporal requirement of ROI that the horizontal magnetic field should increase over 100 G during the time interval from the flare onset to the end of flare end is empirical. It still remains to be tested whether this is always the case.

The other objective of this paper is to test the relationship between the CME eruption and the change of the horizontal field. Considering the momentum conservation, it is natural to expect that an upward CME will result in a downward momentum impulse, which may lead to a change of magnetic field in the photosphere. According to the model of Fisher et al. (2012), the momentum equation is

$$M_{\text{CME}} v = \frac{1}{2} \delta F_r \delta t, \quad (5)$$

where δF_r is the change of the Lorentz force acting on the photosphere (the absolute value¹² determined by Equation (3)), M_{CME} is the CME mass, and v is the CME speed, both of which are available from the *SOHO* CME catalog (see footnote 10), and δt is the reaction time of the physical process. When using this expression, we grossly assume that the entire mass of the CME moves with the same velocity, and that the work done against gravity is ignored. Another assumption is made that the Lorentz force changes linearly during the time interval δt , which results in a factor 1/2 in Equation (5). Since the theory behind the increase at the penumbra is unclear, we only study the regions of Type I and the R1 regions of Type II. Therefore, the value of “back reaction” time, δt , can be derived from the

¹¹ The mean value is calculated by the average of the measured values at five times instants immediately prior/posterior to the start/end time.

¹² The change of Lorentz force acting on the outward atmosphere and that acting on the interior have the same magnitude, but opposite signs.

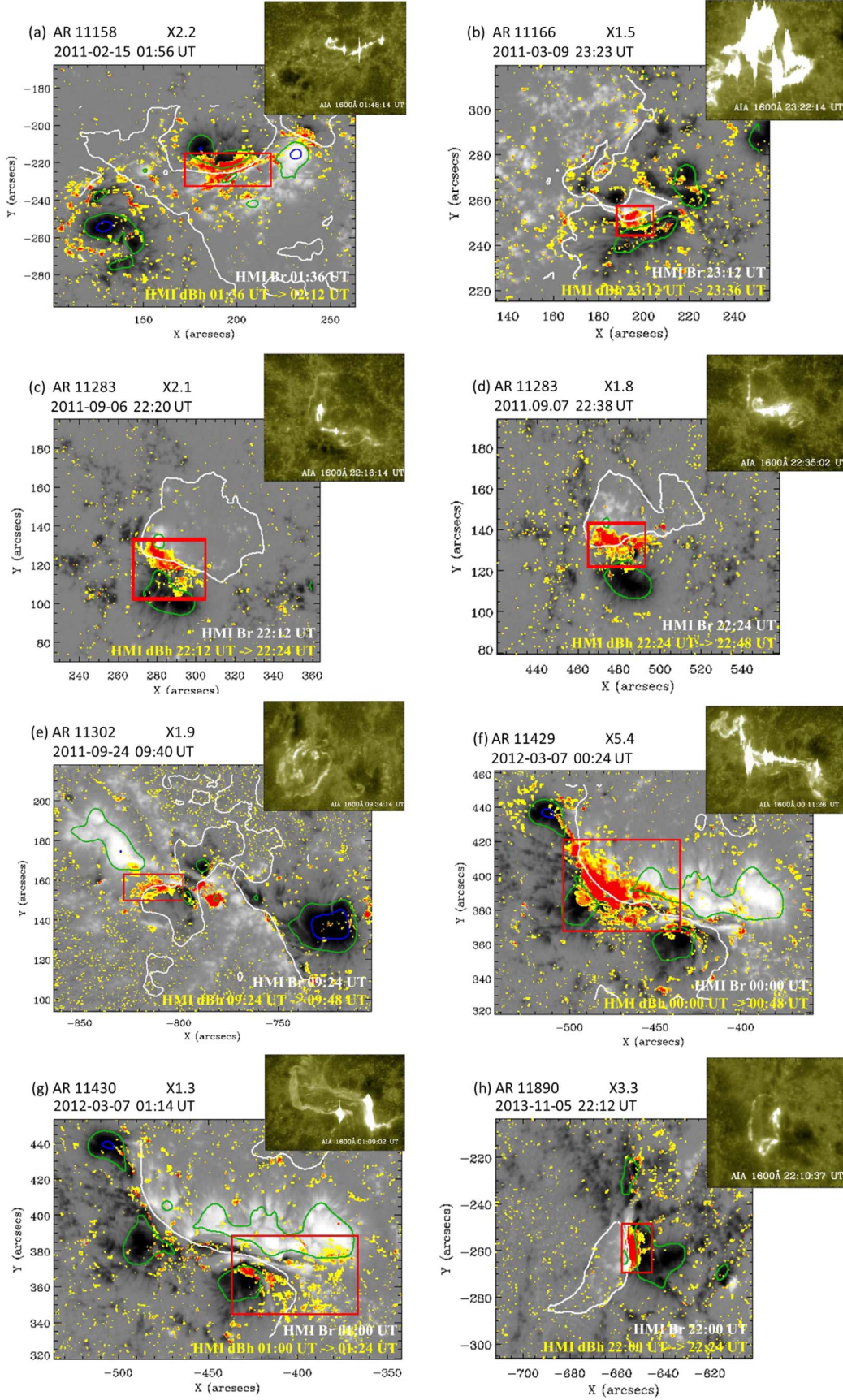


Figure 2. Overview of magnetic imprints in eight X-class flares with heliographic angles no greater than 45° . The notation in each panel is similar to that in Figure 1(a). The B_r maps are all scaled between ± 2000 G. All eight events in panels (a)–(h) are categorized as type I in Section 3.

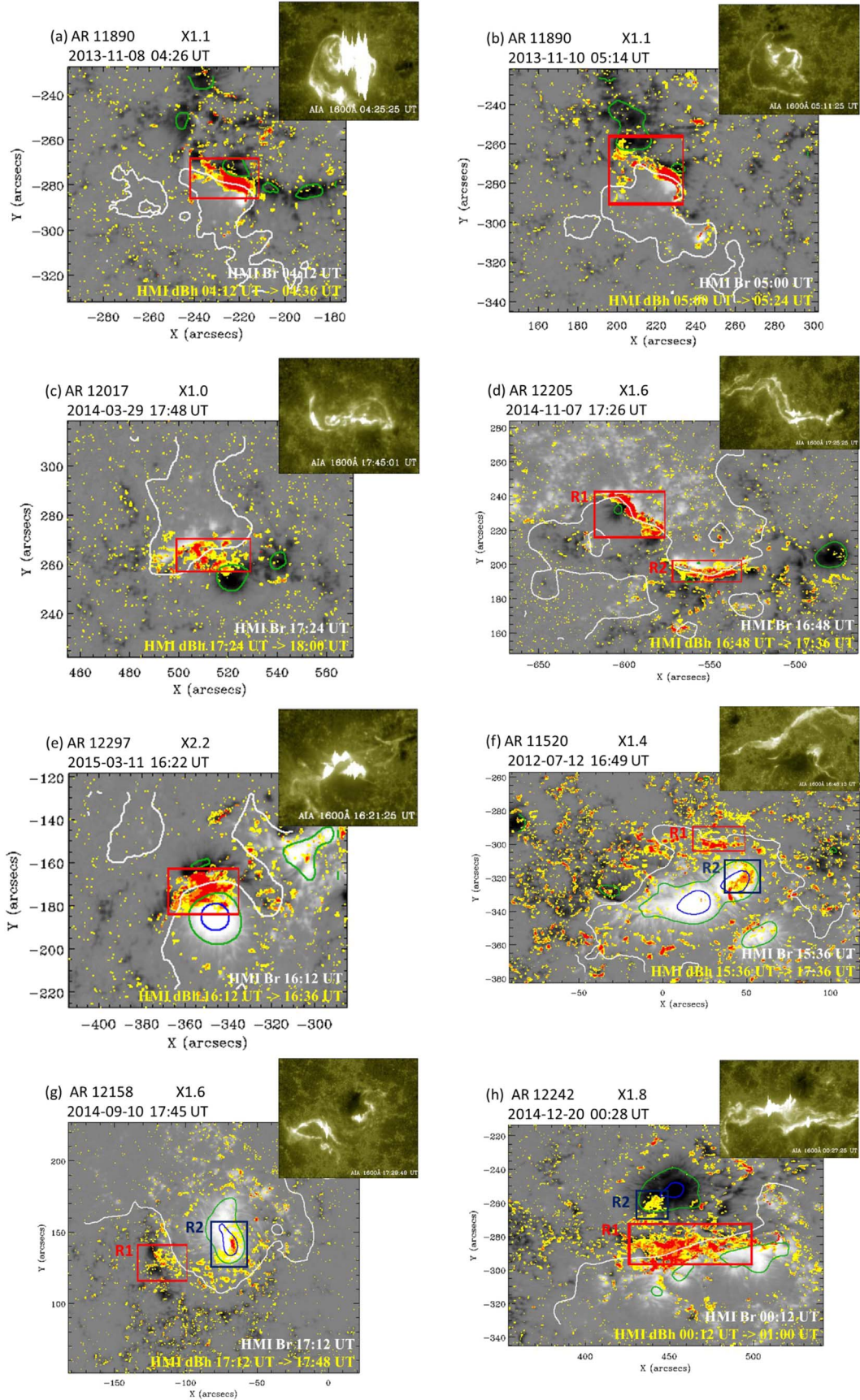


Figure 3. Overview of magnetic imprints in eight X-class flares with heliographic angles no greater than 45° . The notation in each panel is similar to that in Figure 1(a). The B_r maps are all scaled between ± 2000 G. The five events in panels (a)–(e) are categorized as type I in Section 3. The three events in panels (f)–(h) are categorized as type II.

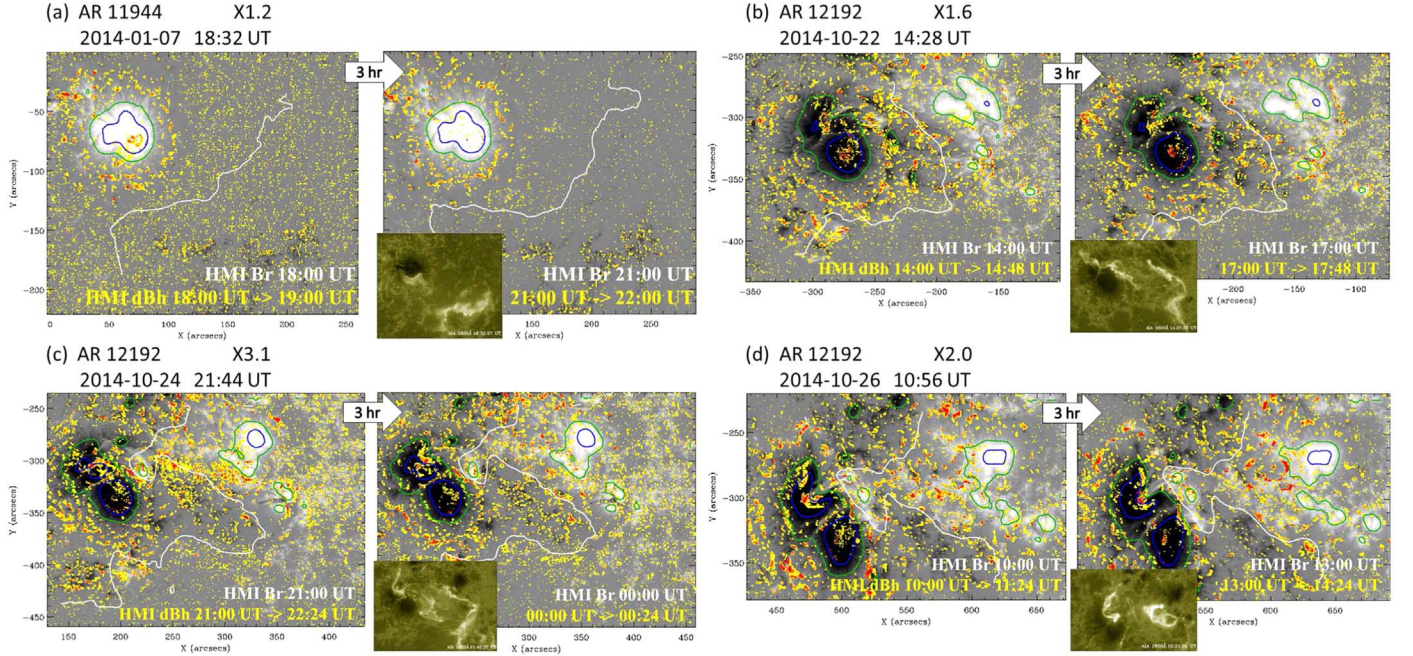


Figure 4. Overview of magnetic imprints in four X-class flares with heliographic angles no greater than 45° . The notation in each panel is similar to those in Figures 1(a), (b), and (d), where the left part shows the difference map of B_r during flare time and the right part shows it in post-flare time (3 hr later). The B_r maps are all scaled between ± 2000 G. The four events in panels (a)–(d) are categorized as type III in Section 3.

linear relationship between the CME momentum and the change of Lorentz force, δF_r , (see Figure 5(c)), whose slope equals $\frac{2}{\delta t}$. The value of δt of our samples is then calculated to be ~ 70 s, with the 90% confidence interval being about 50–90 s. Our estimation of back reaction time is longer than the rough estimation of 10 s given by Wang et al. (2012b). One thing should be pointed out though; in reality, the Lorentz force may not change linearly. If the change is initially more rapid than a linear change, the factor in Equation (5) will be larger than $1/2$; if the change is initially slower than a linear change, the factor will be smaller than $1/2$. This could explain the fairly large dispersion of the data points from the linear fitting in Figure 5(c).

4. Conclusions and Discussion

After a statistical study of a sample of X-class flares with heliographic angles no greater than 45° since *SDO*’s launch, and further quantitative measurement of key parameters related to the magnetic field change, we reach the following main conclusions,

First, most but not all the X-class solar flares would implement magnetic imprints at PIL on the photosphere. In our sample of 20 flares, we observe that the horizontal fields in one flare event in AR 11944 and three flare events in AR 12192 nearly remain unchanged at PIL during the flare time, similar to their behavior in the post-flare time (see Figure 4). Our statistical study aims to explore the question presented by Sun et al. (2017): are the magnetic imprints universal? The four aforementioned Type III examples suggest that the magnetic imprints may not be universal in X-class flares, where categorization of the magnetic imprints is necessary. We still

need to explore whether the universality exists in M-class or C-class flares.

Second, we find that the magnetic imprints of X-class flares are located not only at the PIL (see Wang et al. 2012a; Song & Zhang 2016; Sun et al. 2017) but also at the penumbra in some cases (see Region 2 in Figures 3(e)–(f)); or not at PIL (see Figure 4). This new finding needs to be checked with more observations and awaits a theoretical explanation. We need to clarify how the change at the penumbra is related to the magnetic imprints that are usually found at the PIL, as it is not easily explained by the tether-cutting model (Moore et al. 2001).

Third, we quantitatively evaluate the change of the horizontal field, inclination angle, and time duration of the magnetic imprint process. As is seen in Table 1 and Figure 5, the increase of the horizontal field ranges from 150 to 450 G, and the decrease of the inclination angle ranges from 1° to 10° . These quantitative features constrain the geometrical change of the magnetic field, which has implications for constructing the physical model behind magnetic imprints.

Fourth, we check the change of the Lorentz force on the photosphere in the ROI, which is proportional to integration of the δB_h^2 . We find that this parameter is strongly correlated with the CME momentum (see Figure 5(d)). It suggests that a CME with a higher momentum is associated with a stronger magnetic imprint on the photosphere. In this sense, in the three X-flares in AR 12192, where there is no or very small CME momentum (also called as “confined flares” e.g., Ji et al. 2003), it is natural that we cannot see intensive magnetic imprints. Sun et al. (2015) argued that the CMEs might be restricted by strong background fields. However, in the X-flare in AR 11944, we also cannot see the intensive magnetic imprint, regardless of the very large momentum of the associated CME ($\sim 402.6 \times 10^{17}$ g km s $^{-1}$, the highest among Table 1). This might be because of its

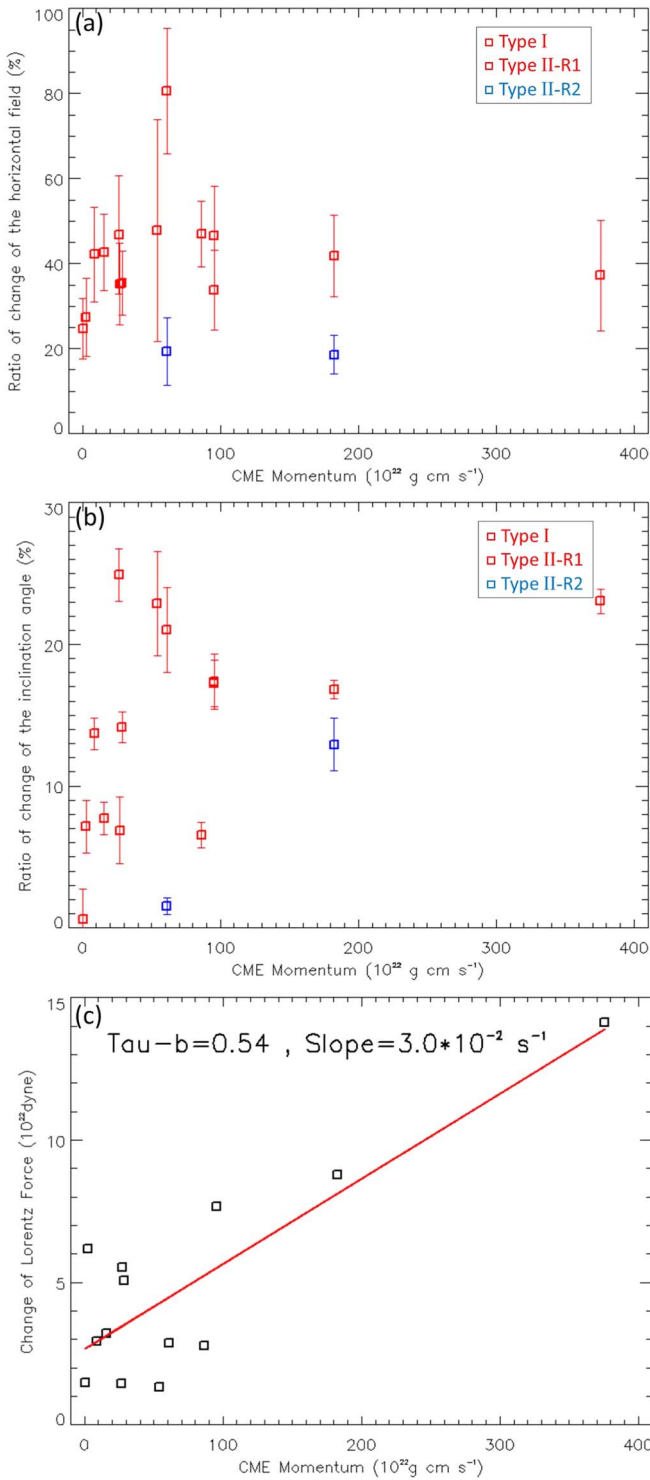


Figure 5. (a) Ratio of change of the horizontal field, with respect to the CME momentum. (b) Ratio of change of the inclination angle. (c) Scatter plots of the CME momentum vs. the change of the Lorentz force, where the non-parametric Kendall's Tau-b coefficient is estimated to be 0.54. The red line shows the linear fitting to the data points, where the slope is estimated to be $3.0 \times 10^{-2} \text{ s}^{-1}$, with the 90% confidence interval being $[2.3, 3.7] (\times 10^{-2} \text{ s}^{-1})$. The uncertainty of the slope is calculated by the bootstrap method with 50,000 iterations.

complex magnetic structure and unusual CME motion (Möstl et al. 2015; Wang et al. 2015). Moreover, we have estimated the back reaction time to be $\sim 70 \text{ s}$. As first introduced by Wang et al. (2012b), because we can calculate δF_r and measure the CME

speed, v , once we know the key parameter back reaction time δt , we are able to estimate the CME mass. Based on the above analysis, we provide $\delta t \sim 70 \text{ s}$ as a reference value for such CME mass estimation. Here, the back reaction process is triggered by the magnetic reconnection, during which CME is propelled outward. The back reaction time, $\sim 70 \text{ s}$, is shorter than the stepwise evolution time of the horizontal field on the photosphere, which is typically $\sim 48 \text{ minutes}$. Nevertheless, the physical nature of the reaction process is still unclear. In the future, we need to check the observational data with even higher cadence (Sun et al. 2017), and perform MHD simulations for the eruptions, to understand the reaction process.

We are very grateful to the referee for constructive comments that helped improve the paper. We thank Kai Yang for help in data processing, and Xudong Sun for valuable comments on the manuscript. This project was supported by NSFC under grants 11733003, 11773016, 11703012, and 11533005, and NKBRF under grant 2014CB744203.

ORCID iDs

Zekun Lu <https://orcid.org/0000-0001-7961-7617>
Yining Zhang <https://orcid.org/0000-0001-5933-5794>
Mingde Ding <https://orcid.org/0000-0002-4978-4972>
Yang Guo <https://orcid.org/0000-0002-9293-8439>

References

- Bobra, M. G., Sun, X., Hoeksema, J. T., et al. 2014, *SoPh*, **289**, 3549
Fisher, G. H., Bercik, D. J., Welsch, B. T., & Hudson, H. S. 2012, *SoPh*, **277**, 59
Hagenaar, H. J., & Shine, R. A. 2005, *ApJ*, **635**, 659
Hoeksema, J. T., Liu, Y., Hayashi, K., et al. 2014, *SoPh*, **289**, 3483
Hong, J., Ding, M. D., Li, Y., & Carlsson, M. 2018, *ApJL*, **857**, L2
Hudson, H. S. 2000, *ApJL*, **531**, L75
Iida, Y., Hagenaar, H. J., & Yokoyama, T. 2012, *ApJ*, **752**, 149
Ji, H., Wang, H., Schmahl, E. J., Moon, Y.-J., & Jiang, Y. 2003, *ApJL*, **595**, L135
Kopp, R. A., & Pneuman, G. W. 1976, *SoPh*, **50**, 85
Leka, K. D., Barnes, G., Crouch, A. D., et al. 2009, *SoPh*, **260**, 83
Lemen, J. R., Title, A. M., Akin, D. J., et al. 2012, *SoPh*, **275**, 17
Liu, C., Deng, N., Liu, R., et al. 2015, *ApJL*, **812**, L19
Liu, Y., Hoeksema, J. T., Scherrer, P. H., et al. 2012, *SoPh*, **279**, 295
Masson, S., Parlat, E., Aulanier, G., & Schrijver, C. J. 2009, *ApJ*, **700**, 559
Masson, S., Parlat, É., Valori, G., et al. 2017, *A&A*, **604**, A76
Metcalf, T. R. 1994, *SoPh*, **155**, 235
Moore, R. L., Sterling, A. C., Hudson, H. S., & Lemen, J. R. 2001, *ApJ*, **552**, 833
Möstl, C., Rollett, T., Frahm, R. A., et al. 2015, *NatCo*, **6**, 7135
Pesnell, W. D., Thompson, B. J., & Chamberlin, P. C. 2012, *SoPh*, **275**, 3
Petric, G. J. D. 2012, *ApJ*, **759**, 50
Petric, G. J. D. 2013, *SoPh*, **287**, 415
Scherrer, P. H., Schou, J., Bush, R. I., et al. 2012, *SoPh*, **275**, 207
Song, Y., & Zhang, M. 2016, *ApJ*, **826**, 173
Sudol, J. J., & Harvey, J. W. 2005, *ApJ*, **635**, 647
Sun, X., Bobra, M. G., Hoeksema, J. T., et al. 2015, *ApJL*, **804**, L28
Sun, X., Hoeksema, J. T., Liu, Y., et al. 2012, *ApJ*, **748**, 77
Sun, X., Hoeksema, J. T., Liu, Y., Kazachenko, M., & Chen, R. 2017, *ApJ*, **839**, 67
Wang, H. 1992, *SoPh*, **140**, 85
Wang, H., Ewell, M. W., Jr., Zirin, H., & Ai, G. 1994, *ApJ*, **424**, 436
Wang, H., & Liu, C. 2012, *ApJ*, **760**, 101
Wang, H., Spirock, T. J., Qiu, J., et al. 2002, *ApJ*, **576**, 497
Wang, R., Liu, Y. D., Dai, X., et al. 2015, *ApJ*, **814**, 80
Wang, S., Liu, C., Liu, R., et al. 2012a, *ApJL*, **745**, L17
Wang, S., Liu, C., & Wang, H. 2012b, *ApJL*, **757**, L5
Yang, K., Guo, Y., & Ding, M. D. 2015, *ApJ*, **806**, 171
Ye, D.-D., Liu, C., & Wang, H. 2016, *RAA*, **16**, 95